Irregular lattice model for quasistatic crack propagation

J. E. Bolander* and N. Sukumar[†]

Department of Civil and Environmental Engineering, University of California, Davis CA, 95616
(Received 13 June 2004; revised manuscript received 16 December 2004; published 24 March 2005)

An irregular lattice model is proposed for simulating quasistatic fracture in softening materials. Lattice elements are defined on the edges of a Delaunay tessellation of the medium. The dual (Voronoi) tessellation is used to scale the elemental stiffness terms in a manner that renders the lattice elastically homogeneous. This property enables the accurate modeling of heterogeneity, as demonstrated through the elastic stress analyses of fiber composites. A cohesive description of fracture is used to model crack initiation and propagation. Numerical simulations, which demonstrate energy-conserving and grid-insensitive descriptions of cracking, are presented. The model provides a framework for the failure analysis of quasibrittle materials and fiber-reinforced brittle-matrix composites.

I. INTRODUCTION

The use of discrete, one-dimensional elements to represent structural continua dates back to the work of Hrennikoff.[1] The modern counterparts of such discrete systems are lattice models, which are composed of simple, one-dimensional mechanical elements connected on a dense set of nodal sites that are either regularly or irregularly distributed.[2] These models have their primary justification in the physical structure of matter at a very small scale, where material can be seen as a collection of particles in equilibrium with their interaction forces. Lattice models have also been used to study the behavior of a variety of materials at larger scales, with particular interest in their disorder and breakdown under loading.[2,3]

When subjected to loading, the lattice network has elastic strain energy $\mathcal{H}(\mathbf{u})$, where $\mathbf{u} = \{\mathbf{u}_1, \ldots, \mathbf{u}_N\}$ are the generalized displacements of the N nodal sites. On minimizing $\mathcal{H}$ with respect to $\mathbf{u}$, a system of equations is obtained, from which $\mathbf{u}$ is determined. The breaking of an element in a lattice network is based on criteria in terms of element strain, generalized force, or energy, as determined from the displacement solution. In the classical approach, an element is removed from the network if it meets the breaking criterion. The procedure is repeated, where only the most critical element is removed for each solution of the equation set. Loading on the network is incremented only after all elements are within the limits set by the breaking criterion.

Lattice models differ mainly in the manner in which neighboring nodal sites interact via the lattice elements. With respect to modeling material fracture, the simplest and one of the most popular forms of interaction is through central force (or axial) springs.[4–6] A more general form of interaction is provided by the Born model,[7] which includes both axial and transverse stiffnesses, although this model in not rotationally invariant. With the introduction of rotational degrees of freedom at the element nodes, bond-bending,[8] granular, and Euler-Bernoulli beam[9,10] models overcome the deficiency of the Born model and allow for a more general interaction between the neighboring sites that, in the limit, relate to a gradient continuum, such as Mindlin-Toupin or Cosserat

continua. A gradient continuum includes higher-order terms and an internal length scale, which are absent in the continuum theory of linear elasticity. By virtue of nodal site symmetry, lattices formed from regularly positioned nodal sites can model uniform straining. However, regular lattices tend to provide low energy pathways for element breaking and, therefore, can strongly bias the cracking direction. Irregular lattices[11,12] exhibit less bias on cracking direction and offer freedom in domain discretization, yet generally do not provide an elastically uniform description of the material.

In this paper, we utilize beam-type elements in an irregular lattice model of fracture for quasibrittle materials such as concrete composites. The scaling of element stiffness terms is based on a Voronoi discretization of the material domain and provides an elastically uniform description of the material under uniform modes of straining. This Voronoi scaling was introduced by Christ *et al.*,[13] who investigated the possibility of carrying out quantum field theory computations using a random lattice. The elastically uniform lattice serves as a basis for the explicit modeling of heterogeneous features, such as inclusions and fibers. Fracture is modeled using a cohesive description of cracking. Closing pressures associated with the cohesive crack law blunt the singularity that would exist at the crack tip in linear elastic fracture mechanics. This reduces nodal rotations that might otherwise accentuate differences between theories based on gradient continua and classical linear elasticity. In contrast to most lattice models, element breaking is gradual and governed by rules that provide an energy conserving, objective representation of fracture through the irregular lattice.

Numerical examples are presented to demonstrate the accuracy and applicability of the lattice model in terms of its elasticity and fracture properties. These capabilities provide an effective framework for the modeling of fracture in heterogeneous materials. For instance, the lattice model proposed herein can serve as a basis for modeling fracture in fiber-reinforced brittle-matrix composites and in other multiphase materials when each phase is assumed to be homogeneous.
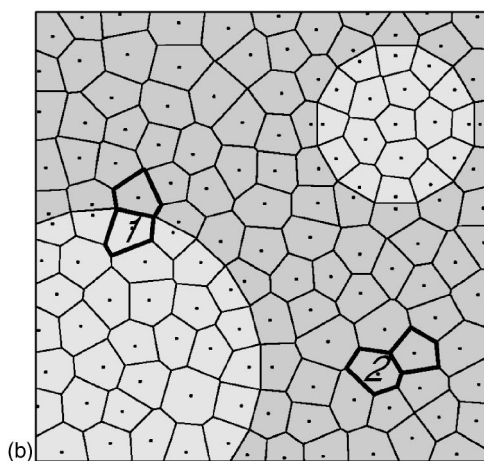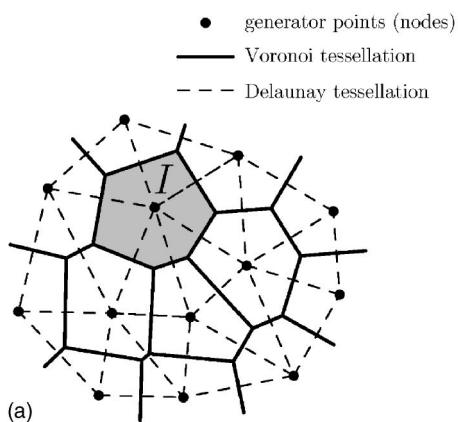
FIG. 1. (a) Dual tessellations of a two-dimensional set of points and (b) Voronoi diagram partitioning of a multiphase material.

II. DOMAIN DISCRETIZATION

The elastic properties of the material are discretized using a Voronoi diagram on an irregular set of points.[14] By definition, the Voronoi cell associated with site *I* is the set of points closer to site *I* than all other sites in the domain [Fig. 1(a)]. The Voronoi partitioning of the material domain is robust and facilitates a high degree of preprocessing automation. Advantages of this approach include the ability to do the following:

(1) Explicitly model material structure, such as the boundaries between two phases (which generally do not run along the grid lines produced by a regular triangular or square lattice). This can be done by strategically placing semiregularly spaced points prior to random filling of the domain [Fig. 1(b)].

(2) Grade average cell size (grid point density), which can be advantageous for improving resolution in critical regions of the domain, while reducing computational expense elsewhere.

(3) Perform adaptive mesh refinement in nonlinear or time-dependent problems.

In the following, the generator points of the Voronoi diagram are the lattice sites (nodes), whereas the edges of the corresponding Delaunay triangulation define the lattice element connectivities [Fig. 1(a)]. For the planar analyses considered
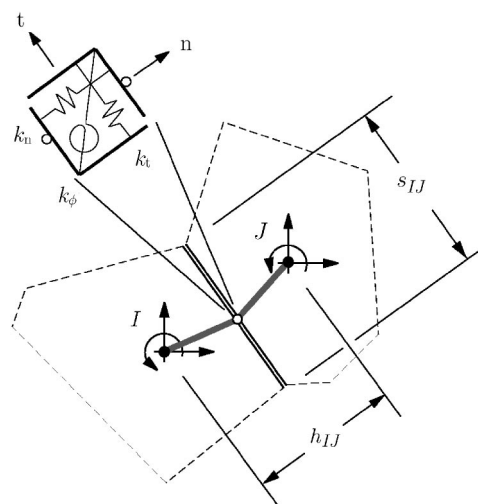

FIG. 2. Basic element of the spring network model.

here, two translational and one rotational degrees of freedom are defined at each lattice node.

III. LATTICE ELEMENT DESCRIPTION

A. Elasticity model

The lattice element, shown in Fig. 2, consists of a zero-size spring set that is connected to the lattice nodes via rigid arms. The spring set is positioned at the midpoint of the Voronoi edge common to the two nodes. This general approach has evolved from the rigid-body-spring concept of Kawai.[15,16] Each spring set consists of normal, tangential, and rotational springs that are defined as local to the common edge and assigned stiffnesses k_n, k_t, and k_ϕ, respectively. These stiffnesses are simple functions of the distance, h_{IJ}, between the lattice nodes *I* and *J* and the length of the common Voronoi edge, s_{IJ},

$$k_n = EA_{IJ}/h_{IJ},$$

$$k_t = EA_{IJ}/h_{IJ}, \qquad (1)$$

$$k_\phi = k_n s_{IJ}^2/12,$$

where $A_{IJ} = s_{IJ}t$, with *t* being the thickness of the planar model and *E* being the elastic modulus of the continuum material. The systematic scaling of the spring stiffnesses given in Eq. (1) provides an elastically homogeneous representation of the continuum,[15,17] which is necessary for the objective modeling of fracture described later in this work. The same s_{IJ}/h_{IJ} scaling relation has been used for random walks on arbitrary sets[18] and for solving two-dimensional and three-dimensional diffusion problems on irregular grids.[19,20] Lattice models are limited in their ability to represent Poisson effects in linear elasticity, due to the unidirectional structure of the lattice elements. A limited range of macroscopic Poisson ratios can be modeled by the regular arrangement of lattice elements or by the adjustment of element stiffness coefficients, but a local realization of the Poisson effect is not obtained. The proposed model can represent

a range of macroscopic Poisson ratios by setting $k_t = \alpha k_n$, where $0 \leq \alpha \leq 1$, but for $k_t \neq k_n$ the material model is not elastically homogeneous.[17] Schlangen and Garboczi[10] provide an alternative approach to obtaining an elastically uniform random lattice, which involves the iterative refinement of the lattice element properties.

Due to the arrangement of its six nodal degrees of freedom, the element shown in Fig. 2 is similar to a beam-spring element with axial stiffness, such as those used by Schlangen and van Mier[21] to model elasticity and brittle fracture at the material scale. For the special case of a square lattice, the two approaches provide the same element stiffness matrices,[15] provided the s_{IJ}/h_{IJ} scaling is also used for the beam element properties. In general, however, the stiffness formulations are different, partly because the spring set is located eccentrically to the element axis (Delaunay edge) so that elemental axial and rotational stiffness terms are coupled.

B. Fracture model

One motivation for utilizing lattice models is the explicit representation of discontinuous material structure at fine scales, including the simulation of bond breaking in atomic structures. At coarser resolutions, however, the model represents the material as a continuum. Heterogeneity is introduced into the network either explicitly or through statistical variations in the element properties.[2] As a fundamental requirement for either case, the lattice formulation must be able to provide an unbiased representation of fracture through a homogeneous medium. Consider the discretization of a two-phase composite shown in Fig. 1(b). At this scale, heterogeneity is apparent at the junction of different phases, whereas each phase by itself is often regarded as a homogeneous material. From a modeling perspective, the lattice elements either (1) correspond to specific features of the material structure, such as an interface between different phases or (2) are not related to any material feature, such as when representing homogeneous properties within a single phase. The proposed lattice model is applied to the latter of these two cases, although the approach can be tailored to treat both cases.

In this study, mode I cracking is simulated by degrading the strengths and stiffnesses of the lattice elements, according to the crack-band approach.[22] The crack-band model is based on the observation that microcracking, crack branching, and other toughening mechanisms associated with cracking occur within a fracture process zone, the width of which is typically related to the maximum size of the heterogeneities. These various crack openings are assumed to be uniformly distributed over the crack-band width. In the numerical implementation of the model, cracks form and propagate through the element interiors and the band width generally conforms to the element size, rather than to the actual width of the fracture process zone (i.e., the fracture localizes into the smallest width permitted by the element discretization of the material domain, provided there is no artificial locking of the crack opening that might otherwise cause the crack band to widen). In this sense, the crack-band
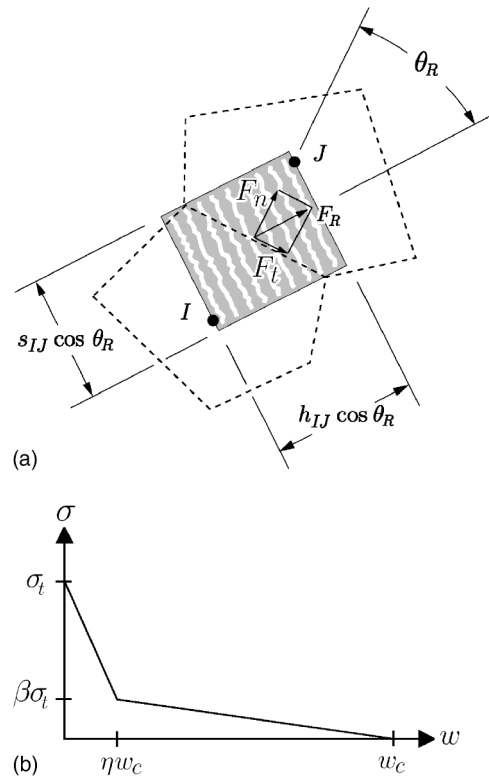

FIG. 3. (a) Crack-band geometry within an element of the spring network model and (b) associated softening relation.

model is functionally equivalent to the cohesive crack model, as considered by Dugdale[23] and Barenblatt[24] and later applied to softening materials by Hillerborg *et al.*[25] According to this type of fracture model, separation takes place across a cohesive zone and is resisted by cohesive tractions. Within this framework, the physically unrealistic $\sqrt{r}$ singularity that arises in linear elastic fracture mechanics[26] is avoided. For brittle materials, the interface traction law can be linked with the gradual breaking of atomic bonds toward the formation of a new traction-free surface. The area under the traction-displacement curve is the specific fracture energy, G_F, and the maximum effective stress, σ_t, the maximum effective separation, w_c, and the shape of the traction-displacement curve are material parameters. When cohesive tractions diminish with increasing separation, the traction-displacement curve can be referred to as a softening relation.

An important feature of the fracture model is that the crack band can form at an angle θ_R to the element axis and the dimensions of the crack band are determined according to the local geometry of the Voronoi diagram[17] [Fig. 3(a)]. The forces carried by the spring sets are known at any stage of the loading history. An average value of tensile stress can be calculated from the resultant of this force pair, divided by the projected area,

$$\sigma_R = \frac{F_R}{A_{IJ} \cos \theta_R}. \tag{2}$$

To obtain proper fracture energy consumption for different meshing strategies, strain values characterizing the softening response are[22]

$$\varepsilon^{cr} = \frac{w}{h_{IJ} \cos \theta_R}, \qquad (3)$$

where w is the crackopening displacement, which is assumed to be uniformly distributed over the crack-band width of $h_{IJ} \cos \theta_R$ [Fig. 3(a)]. In essence, mode I cracking is controlled by the shape of the tension-softening diagram and the fracture energy, G_F, which are assumed to be material properties and thus do not depend on the domain discretization. The softening diagram, shown in Fig. 3(b), can be defined by stress and crack-opening values determined through inverse analysis of fracture test results.[17] After each load increment, the resultant tensile stress in each spring set is checked against the softening relation. For a critical spring set, fracture involves an isotropic reduction of the spring stiffnesses and an associated release of spring forces, so that the resultant stress lies on the corresponding softening relation. The release of spring forces causes an imbalance between the external and internal nodal force vectors, which often promotes additional fracture within the load step. The process of partially breaking the single most critical element and then solving the associated system of linear equations is repeated within each load step until the fracture criterion is satisfied throughout the problem domain. Although this process is computationally demanding, negative stiffness terms are avoided and zero-energy modes of deformation are not produced.

IV. NUMERICAL SIMULATIONS

A. Elastic uniformity of irregular lattices

In Fig. 4, quasiuniform and graded discretizations of a unit square domain are illustrated. For uniform strain conditions imposed on the boundaries, the lattice sites should displace so that uniform strain occurs throughout the lattice. Regular lattice models, by virtue of site symmetry, exhibit such elastic uniformity, whereas irregular lattices are generally not elastically uniform.[10]

The lattices indicated in Fig. 4 are subjected to both uniform stretching ($u_1 = x_1$; $u_2 = 0$) and combined stretching and shear ($u_1 = u_2 = x_1 + x_2$). The numerical solution accurately represents the theoretical displacement field, as indicated by the small relative errors indicated in Table I. The relative error is defined as

$$e_r = \frac{\|\mathbf{u} - \mathbf{u}^h\|_2}{\|\mathbf{u}\|_2}, \quad \|\mathbf{u}\|_2 = \sqrt{\sum_{I=1}^{N} \mathbf{u}(\mathbf{x}_I) \cdot \mathbf{u}(\mathbf{x}_I)}, \qquad (4)$$

where $\|\cdot\|_2$ is the L_2 norm of the indicated argument, $\mathbf{u}$ and $\mathbf{u}^h$ are the exact and numerical solutions, respectively, and N is the total number of nodes. The networks do not exhibit spurious heterogeneity arising from either random mesh geometry or varying element size. If each of the lattice elements is assigned a constant area, equal to the average of the Voronoi facet areas $\overline{A_{IJ}}$, then the lattices are not elastically uniform, as evidenced by the large relative errors given in Table I. In producing the results for shear loading, rotations of the
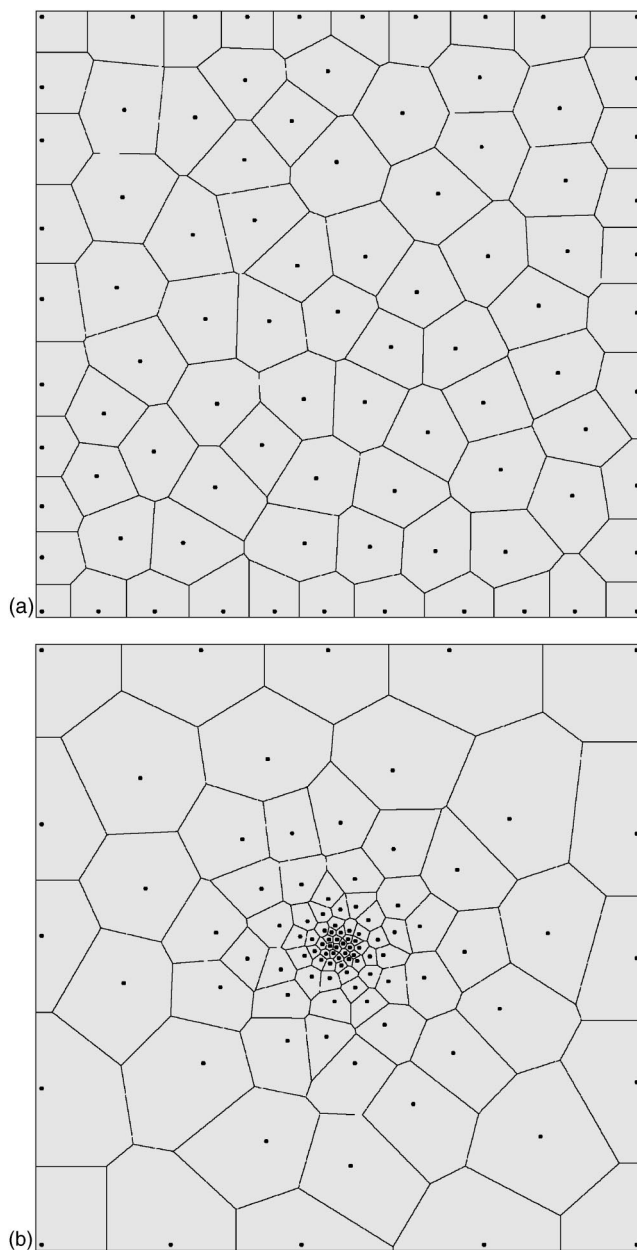

(a)

(b)

FIG. 4. Irregular lattices. (a) Quasiuniform nodal discretization and (b) graded nodal discretization.

Voronoi cells have been constrained for both sets of analyses. The placement of nodes along the boundaries is only to facilitate the analyses and is not a requirement here.

B. Elastic analysis of fiber composites

To illustrate the importance of elastic uniformity, we first consider a short fiber embedded within an irregular lattice model of a matrix material. A fiber contributes to the stiffness of a lattice element if it crosses the common boundary of the two Voronoi cells (Fig. 5). To model this stiffness contribution, a zero-length spring connects the two cells at the boundary crossing. The spring is aligned in the fiber direction and assigned axial stiffness,

TABLE I. Relative errors e_r for uniform strain loading.

Boundary conditions	Quasiuniform mesh		Graded mesh	
	Voronoi scaling	$A_{IJ} = \overline{A_{IJ}}$	Voronoi scaling	$A_{IJ} = \overline{A_{IJ}}$
$u_1 = x_1$ $u_2 = 0$	1.25×10^{-7}	4.41×10^{-2}	5.46×10^{-8}	8.68×10^{-2}
$u_1 = x_1 + x_2$ $u_2 = x_1 + x_2$	1.602×10^{-7}	3.640×10^{-2}	1.191×10^{-7}	7.610×10^{-2}

$$k_f = \frac{A_f \sigma_f(x_c)}{(h_v / \cos \psi) \varepsilon_m}, \qquad (5)$$

where A_f is the fiber cross-section area, ε_m is the matrix strain in the fiber direction, $\sigma_f(x_c)$ is the fiber axial stress at the boundary crossing, and ψ is the angle between the fiber axis and the direction of loading on the composite. The spring stiffness is linked to the computational degrees of freedom, which are defined at the lattice nodes, by assuming the cells to be rigid. The approach is general in that any appropriate model relating $\sigma_f(x_c)$ and ε_m can be used to de-
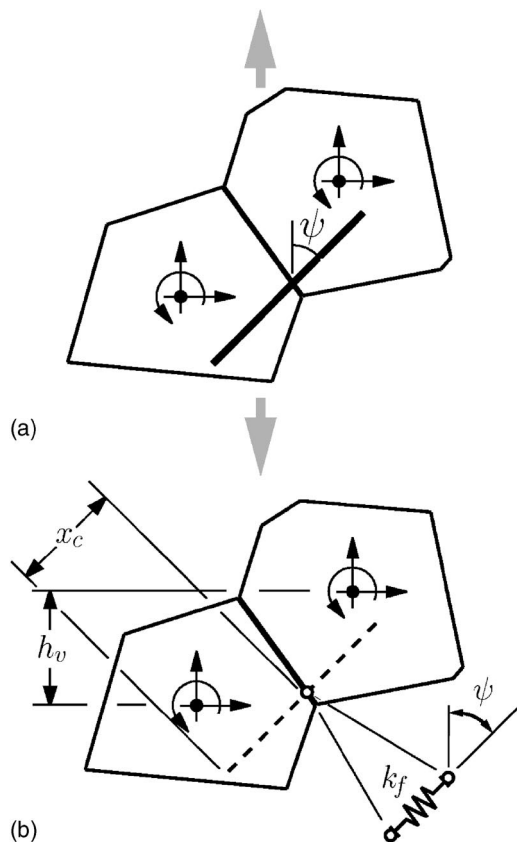

(a)

(b)

FIG. 5. (a) Lattice element with fiber inclusion and (b) fiber contribution to element stiffness.

termine k_f through Eq. (5). The relation used here, and plotted in Fig. 6(b), is based on an elastic shear lag theory pro-

posed by Cox,[27] in which perfect bonding is assumed between the fiber and matrix.

In general, fibers cross multiple Voronoi cell boundaries and therefore contribute to the stiffness and internal force calculations of multiple lattice elements. Figure 6(a) shows a single, inclined fiber of length l_f embedded in a homogeneous matrix subjected to uniaxial tension. The fiber elastic modulus is $E_f = 10 E_m$, where E_m is the elastic modulus of the matrix. For comparisons with Cox's theory,[27] which assumes a uniform strain in the matrix, the fiber diameter is chosen to be small relative to the thickness of the matrix. Axial stress levels in the fiber at each cell boundary crossing are shown in Fig. 6(b), where the axial stress has been normalized by $\bar{\sigma}_f = E_f \varepsilon \cos^2 \psi$, with ε being the strain in the loading direction. The computed axial stress values agree with theory when the Voronoi scaling of the lattice stiffness coefficients is used. The constant-area scaling does not provide an elastically uniform representation of the matrix, and the associated artificial heterogeneity of the lattice is manifested as noise in the axial stress profile.

As a second example, we consider a fiber composite with a random distribution of short fibers. Fibers are randomly inserted in a $a \times a$ square domain with thickness $a/10$ [Fig. 7(a)]. The matrix discretization is shown in Fig. 6(a). The fiber length $l_f = a/8$, fiber diameter $\phi = l_f / 100$, $E_f = 10 E_m$, and 6 519 fibers are used to achieve a fiber volume fraction of 1%. The composite system is subjected to tensile loading in the vertical direction and the fiber axial stress values (for each individual fiber at each boundary crossing) are plotted in Fig. 7(b). Once again the numerical results for the axial stress in the fibers are in good agreement with Cox's theory.[27] Of the 11 497 data points shown in Fig. 7(b), a few stress values differ from the theoretical predictions, since nonuniformity and the discrete nature of the fiber distribution causes variations in the stiffness and therefore fluctuations in strain. Similarly, good agreement with theory is obtained for severalfold increases in the fiber volume fraction, although for much higher fiber contents (or for significantly larger fibers relative to the domain thickness), the heterogeneity more strongly affects straining of the matrix and therefore the axial strain profiles of the fibers. The modeling of local interaction effects between the fibers is approximate, and therefore the physical interpretation of the results also becomes difficult for high volume fractions of fibers.

C. Fracture of uniaxial tension specimen

The lattice model is used to simulate fracture in a rectangular panel of homogeneous material under uniaxial tensile
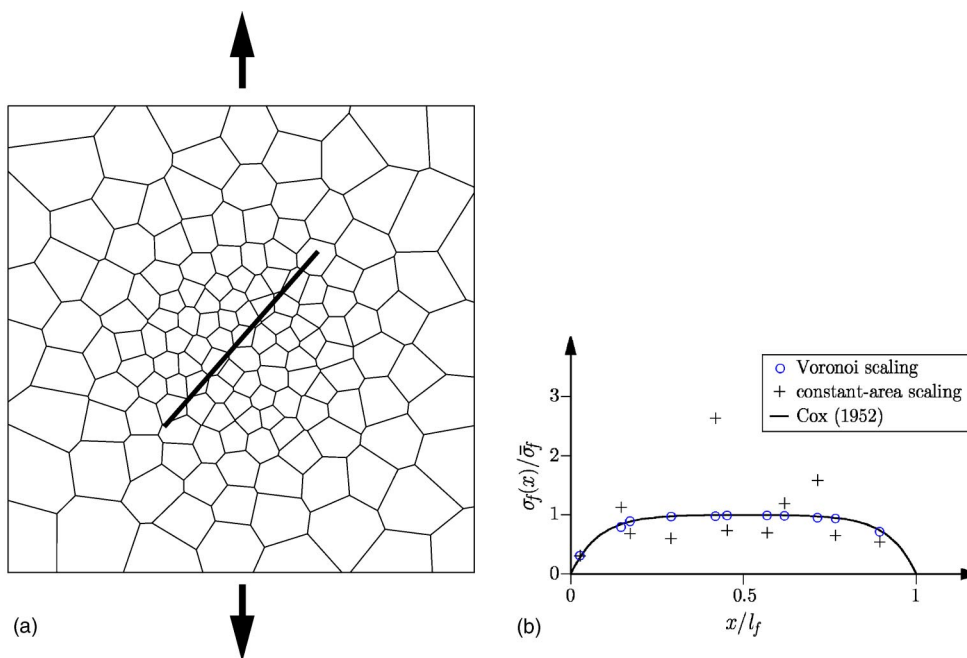
FIG. 6. (a) Inclined fiber in a homogeneous matrix and (b) axial stress along fiber.

loading. The panel has cross-section area A and the softening properties of the material are shown in Fig. 3(b). Figure 8 shows a Voronoi discretization of the panel. For imposed relative displacement δ between the two ends of the specimen (and reactive force P), stress σ_R is determined for each lattice element per Eq. (2); for each element, σ_R has magnitude P/A and acts in the direction of the axial load. With increasing axial load, σ_R reaches the tensile strength σ_t in all elements simultaneously. Only a small reduction of the σ_t value is needed to initiate fracture at any specific location. For a perturbation of $1 \times 10^{-7}\sigma_t$ in the tensile strength of the element at A or B (Fig. 8), fracture initiates at those locations. From the point of crack initiation, fracture propagates through the cross section and the material separates [Figs. 9(a) and 9(b)]. From these plots, it appears that cracking is constrained to follow the intercell boundaries. However, as discussed in Sec. III B, fracture is distributed within the lattice elements and the direction of fracture is not constrained by the discretization. In Fig. 10, average stress $\sigma = P/A$ and axial displacement δ have been normalized to better indicate that the cohesive softening curve [Fig. 3(b)], used as input to the model, is manifested at the structural scale. The separation process involves only two nodes per element; this facilitates the transition from continuous to discontinuous behavior and avoids significant stress locking.

If the crack band is constrained to form normal to the element axis, as would be the case for a central force spring lattice, the model response is not a direct reflection of the softening curve. There are two main sources of error: (1) the magnitude of the stress component aligned with the element axis, $\sigma_n = F_n/A_{IJ}$, is less than the average axial stress $\sigma = P/A$, unless the element is aligned with the direction of tensile loading, and (2) after fracture initiation, the component of crack opening in the direction of the element axis is smaller than that in the direction of loading. These two

sources of error combine to produce excess strength and energy consumption, as indicated by the broken line in Fig. 10, which can be viewed as a form of stress locking. In this case [Fig. 9(c)], fracture initiation does not occur at the point of reduced strength, which happens to be the element at location B. Furthermore, elements at different locations partially fracture prior to localization and ultimate failure along the path shown in Fig. 9(c). Even in most classical lattice approaches,[2] where, upon violation of the fracture criteria, the element is completely removed, the first of these sources of error would still be present. The sensitivity to fluctuations in strength, provided by the elastically uniform material model and the σ_R stress measure, is a prerequisite to analyses based on the statistical assignment of strength values.

D. Fracture of three-point bend specimen

The lattice model is used to simulate the three-point bend test illustrated in Fig. 11. The specimen has dimensions $L = 300$ mm, $d = 100$ mm, $\ell = d/2$, and a uniform thickness of 100 mm. For an actual concrete mix, the physical test[28] provided the load versus crack mouth opening displacement (CMOD) response shown in Fig. 12. Using the regular, straight-line discretization of the potential crack path between the prenotch tip and load application point [Fig. 11(b)], an inverse analysis based on a Levenburg-Marquardt minimization algorithm provided the softening relation parameters ($\sigma_t = 4.12$ MPa, $w_c = 0.154$ mm, $\beta = 0.247$, and $\eta = 0.118$). These softening parameters were then used in a forward analysis to obtain the corresponding load versus CMOD curve in Fig. 12. Differences between the experimental result and the inverse fitting are due, in part, to the use of a bilinear softening relation, which is assumed to be constant during fracture through the ligament length. The dimensions of the three-point bend specimen, boundary conditions, and
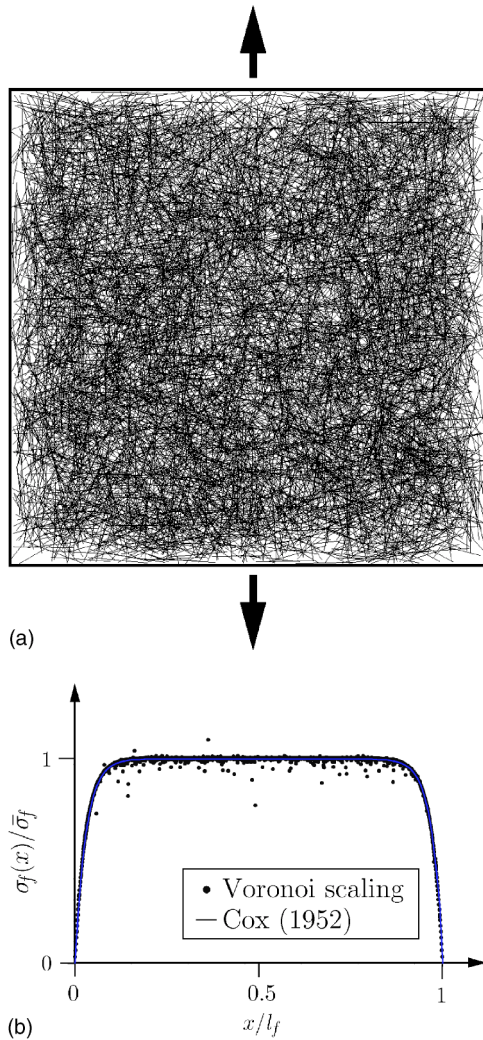
(a)

(b)

FIG. 7. Analysis of random fiber composite. (a) Fiber distribution and (b) axial stress along fibers.

specific fracture energy of the material preclude the appearance of instability in the global load versus CMOD response. The solution process can accommodate instability (such as snap back) in the specimen response by advancing and/or retracting the load point displacements so that the material fracture criterion is precisely followed.

Using the same set of softening parameters, forward analyses are repeated for two different semirandom, irregular discretizations of the ligament length. The deformed mesh at a near-final stage in the loading history for one of the analyses is shown in Fig. 13. The resulting load versus CMOD plots is also given in Fig. 12. The main observation is that mesh size and irregular geometry do not appreciably influence cracking behavior and, therefore, the resulting load-displacement curves agree well.
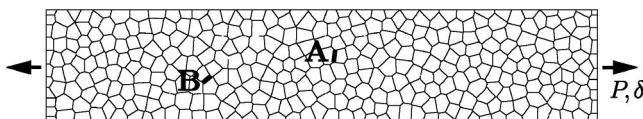

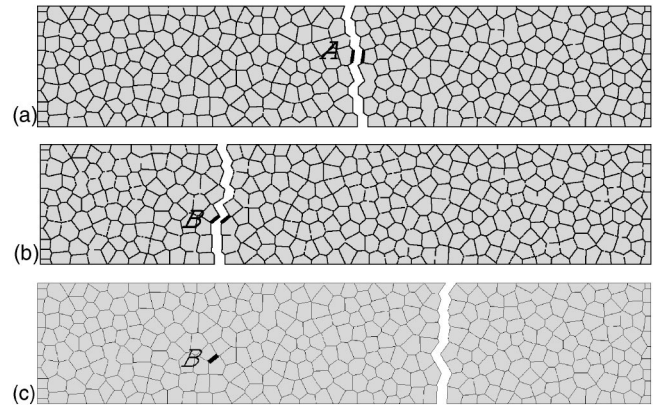FIG. 8. Voronoi discretization of uniaxial tension test specimen.

FIG. 9. Failure patterns (a) Case A, (b) case B, and (c) case B using σ_n fracture criterion.

To help illustrate the consequences of the A_{IJ}/h_{IJ} scaling of the stiffness and crack-band dimensions, two variations are made.

(1) The lattice elements in the fracture ligament region are assigned a constant area, equal to the average of the Voronoi facet areas over the same region. For this case, the initial slope of the load-CMOD diagram is nearly the same, whereas the remainder of the curve is in fair agreement with the previous results (Fig. 14).

(2) As for the uniaxial tension test simulation, the crack band is constrained to form normal to the element axis (i.e., $\sigma_n = F_n/A_{IJ}$ is used to guide fracture). For this case, the global response curve is too tough (Fig. 14). Schlangen and Garboczi[29] have noted a strong directional dependence of the fracture properties of regular lattices when employing this type of normal force fracture criterion.

From these results, it appears that the scaling of the element stiffness terms and the condition of elastic uniformity are of secondary importance when compared to the influence of the element-breaking rules. However, the performance evaluation of the different models should not be based on the global load versus CMOD results alone. The following section focuses on the performance of each model in terms of the rate and variation of energy consumption along the crack trajectory.

E. Energy conservation in crack growth processes

As is common for lattice models, only one lattice element is modified per computational cycle. The energy associated
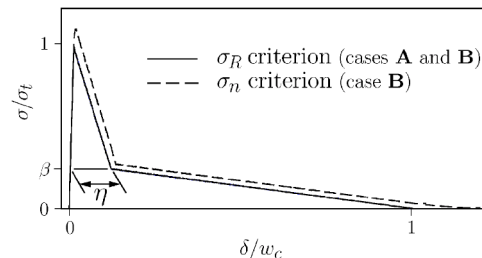

FIG. 10. Normalized load versus displacement relations for simulated uniaxial tension test.
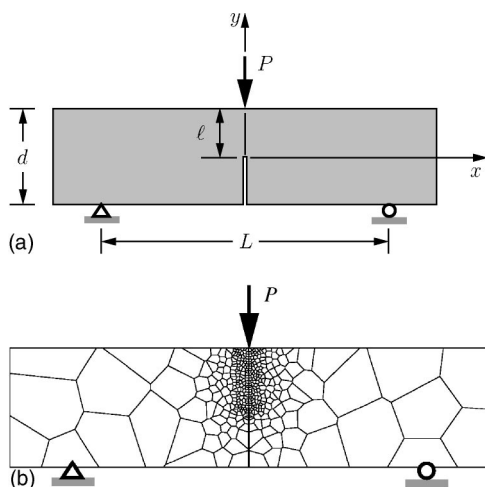
FIG. 11. (a) Three-point bend test specimen and dimensions and (b) Voronoi discretization for inverse analysis of softening parameters.

with the breaking of an element can be computed from the changes in reactive force at the load points, whose displacements are controlled through a finite stiffness device. The cumulative amount of energy consumed by each lattice element is obtained, so that the distribution of local energy consumption can be viewed at any load stage. The total amount of energy assigned to the breaking elements is equal to the difference between the area under the global force versus displacement curve and the elastic strain energy stored in the system.

In Fig. 15, we depict the maps of specific fracture energy consumption, g_F, along the ligament length for the regular and two irregular discretizations of the ligament region. The energies correspond to a near-final stage in the loading history and have been normalized by G_F, the area under the bilinear softening diagram [Fig. 3(b)]. As expected, the regular discretization of the ligament produces uniform energy consumption along the crack trajectory. The ratio g_F/G_F decreases near the top of the ligament length, since w becomes less than w_c and tends to zero when approaching the neutral axis of bending. For the random geometry analysis, the energy distributions are nearly uniform along the principal crack trajectory, with $g_F/G_F \approx 1.0$. Crack propagation through the random mesh produces nearly the same results as crack propagation along a smooth, predefined pathway. This is desirable in that network random geometry does not rep-
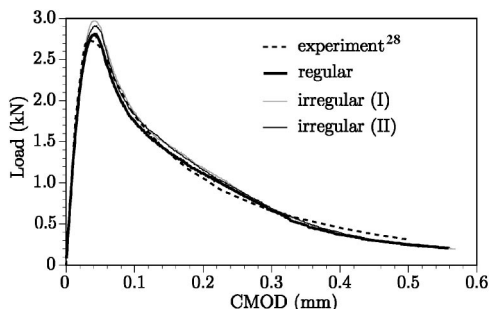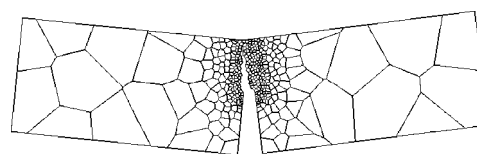

FIG. 13. Mesh for simulating fracture in three-point bend test.

resent any structural features within the material. The simulated uniaxial tension test discussed earlier also exhibits a uniform distribution of $g_F/G_F \approx 1.0$ over the fracture surface.

When using a constant area, $\bar{A}_{IJ}$, for each lattice element in the ligament region, it is clear that local energy consumption does not follow that prescribed by the softening relation [Fig. 16(a)]. For elements with $A_{IJ} > \bar{A}_{IJ}$, the ratio $g_F/G_F < 1$, whereas for elements with $A_{IJ} < \bar{A}_{IJ}$, the converse is true. This tendency for g_F/G_F to be on either side of unity provides reasonable global load-displacement results, as seen earlier in Fig. 14. When constraining fracture to form normal to the element axis (σ_n criterion), however, $g_F/G_F \gtrsim 1$ for all cracks with $w \geq w_c$ [Fig. 16(b)], resulting in overstrength and excess energy consumption in the structural response. The stress locking is more pronounced, relative to that seen for the uniaxial tension specimen, since the fracture path from the prenotch tip includes elements that are significantly inclined to the loading direction. For the uniaxial tension test, there are low energy pathways available, where the elements are closely aligned with the loading direction. In these simulations, there is a temptation to associate the nonuniform distribution of energy consumption with heterogeneous features present in the material. However, the effects of this artificial heterogeneity can be severe and bear no relation to the actual material features.

F. Fracture of fiber-reinforced brittle-matrix composites

The irregular lattice serves as a framework for modeling the fracture of fiber-reinforced brittle-matrix composites. Discontinuous, short fibers are added to brittle matrix materials to provide additional toughness after matrix fracture. The increase in toughness is due to debonding along the fiber-matrix interface, followed by frictional pullout of the fibers traversing an opening matrix crack.[30] Various types of fibers are used, depending on the application, with the fiber

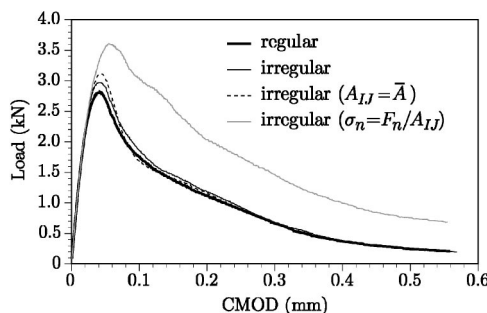FIG. 12. Experimental curve and forward analysis runs.

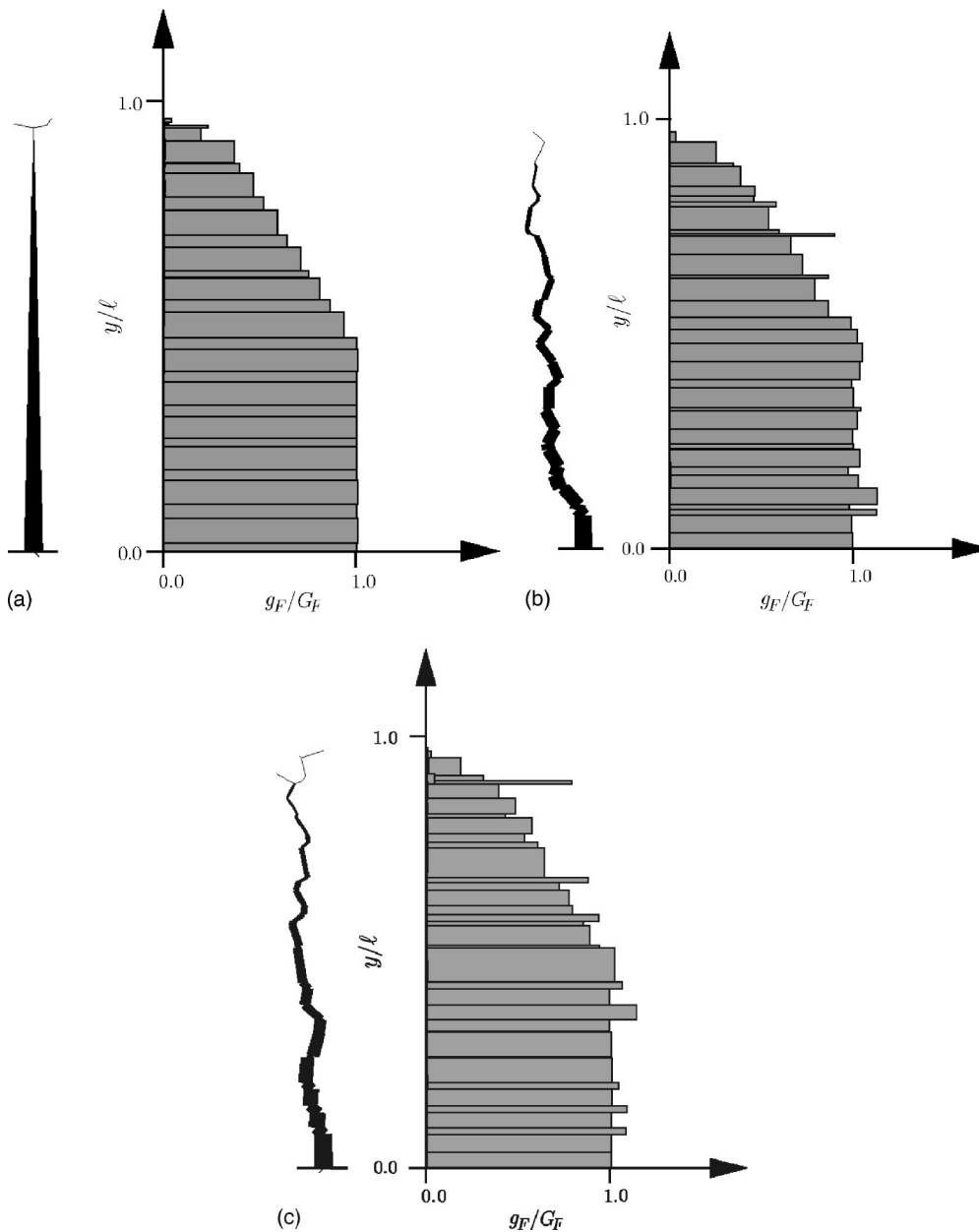FIG. 14. Influence of discretization and fracture criterion on specimen response.

FIG. 15. Crack trajectories and local energy consumption. (a) Regular discretization (b) irregular discretization (case I) and (c) irregular discretization (case II) of the ligament length.

dosages ranging up to several percent by volume of the composite, which is a practical limit for achieving uniform dispersions of fibers with high aspect ratios.

Prior to matrix fracture, fiber contributions to composite stiffness and strength are modeled using elastic-shear lag theory, as described in Sec. IV B. At the onset of matrix fracture, fibers that cross the developing crack are identified, and the associated springs at the crossing locations [Fig. 5(b)] are modified as follows. Considering equilibrium and compatability conditions, the axial stiffness of a modified spring is based on a composite pullout (i.e., axial force versus pullout displacement) curve, which is derived from the pullout relations for the embedded fiber lengths to each side of the spring. The crack opening is modeled as the separation between adjacent Voronoi cells at the fiber-crossing location. The spring aligns with the point of entry of the fiber into each Voronoi cell. With continued crack opening, the shorter embedded length eventually pulls out, whereas the other end

of the fiber unloads after peak fiber load. The pullout relations for each embedded length are derived from the constitutive properties of the matrix-fiber interface [shown in Fig. 17(a), where τ_a and τ_f indicate adhesional and constant frictional bond strengths, respectively]. Slip hardening or frictional decay along the matrix-fiber interface can be considered in the modeling approach. In addition, the spring element is augmented with a beam-spring component to model the flexural and shear properties of the fiber, which become active after fracture initiation. This lumping of the fiber postcracking behavior into a nonlinear spring bridging the crack is valid, provided the fiber crosses only one crack, which is the case in most applications.

Assuming constant $\tau_f = \tau_a$ for the fiber-matrix interface, the direct pullout of a single embedded length from the irregular lattice yields the plot of axial force (at the load point) versus pullout displacement shown in Fig. 17(b). The peak load is equal to $P_0 = \pi \phi l_e \tau_f$, where l_e is the embedded length.
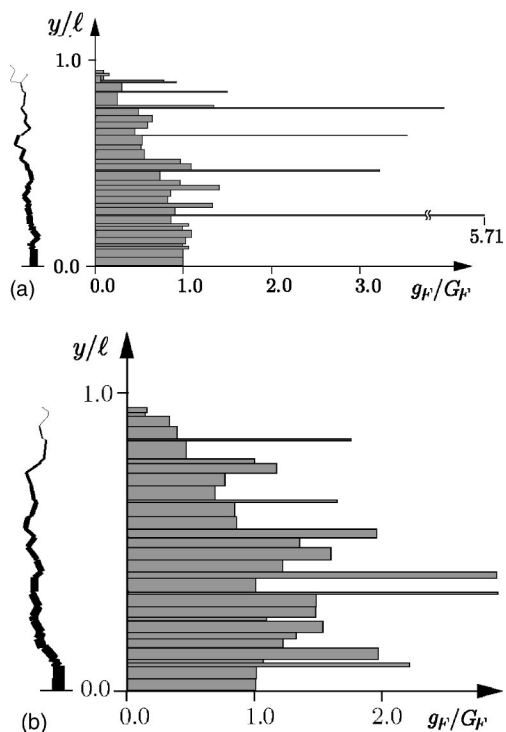
FIG. 18. Axial load versus displacement curves for three nominally identical fiber-reinforced brittle matrix composites.

tioned within an irregular lattice model of a uniaxial tension test specimen. The Voronoi discretization of the $a \times 5a$ rectangular domain (with thickness $a/2$) and the model boundary conditions are as previously shown in Fig. 8. The fiber length $l_f = a/2$, fiber diameter $\phi = l_f/100$, $E_f = 2E_m$, and 2547 fibers are used to achieve a fiber volume fraction of 1%. The matrix-fiber interface is assigned constant bond strength, $\tau = \tau_a = \tau_f$, and $\tau/\sigma_t = 1$. Fiber axial strength is assumed to be greater than the maximum pullout strength ($0.5\pi\phi l_f \tau_f$), so that tensile rupture of the fibers is avoided, which is normally the material design objective.

For the same lattice geometry, three different random realizations of the fiber distribution are considered, providing the three global response curves shown in Fig. 18, where n is the number of fibers bridging the crack and $\bar{l}_e$ is the corresponding average embedded length. The load-displacement response is linear until the onset of matrix fracture, after which the toughening actions of the fibers are mobilized. The response curves are normalized by the mathematically expected postcracking strength,

$$P_e = (\bar{n}\pi\phi l_f/4)\tau_f, \qquad (6)$$

where $\bar{n}$ is the average of n for the three simulations. The scatter in the results is caused by the differences in n and the differences in the distribution of embedded lengths about the expected average of $l_f/4$, both of which are due to random variation in the fiber positions. The load-free crack condition occurs at an axial displacement of $l_f/2$, which corresponds to the maximum possible embedded length. As the postcracking strength is significantly less than the first cracking strength of the composite, a single crack forms, followed by fiber pullout, as shown in Fig. 19. Nonuniformity of the fiber distribution causes variation in the load carried by the matrix; therefore the crack location differs for each of the three simulations.

V. CONCLUSION

In this paper, we have described an irregular lattice model that is suitable for simulating fracture in quasibrittle materials, such as concrete, rock, and other geomaterials. This model differs from previous lattice models in several respects.

FIG. 16. Crack trajectories and local energy consumption. (a) Constant element area ($A_{IJ} = \bar{A}$) and (b) axial stress fracture criterion ($\sigma_n = F_n/A_{IJ}$).

Within the figure inset, the numerical solution is compared with theory[31] for the initial part of the curve that is primarily affected by fiber debonding, i.e., the loss of perfect bond. After peak load, the fiber is completely debonded and the axial force declines linearly due to the loss of embedded length as the fiber is pulled out from the matrix.

To demonstrate and verify the modeling procedure for multiple fiber composites, short fibers are randomly posi-
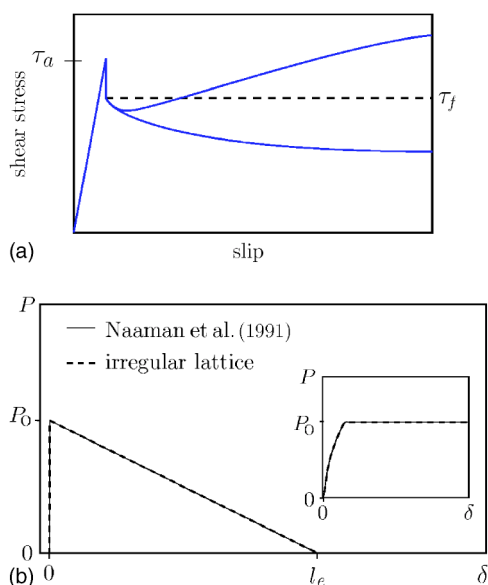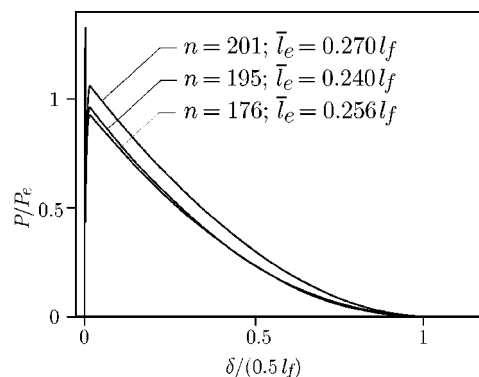

FIG. 17. (a) Constitutive relations for the fiber-matrix interface and (b) axial load versus pullout displacement for a single fiber.
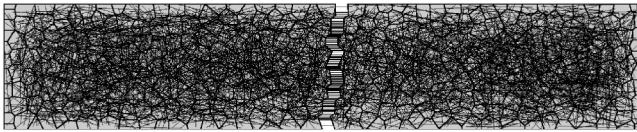
FIG. 19. Fracture localization in the fiber-reinforced composite model.

(1) Lattice geometry is based on a Voronoi discretization of the material domain, allowing effective gradations of nodal point density. The Voronoi diagram provides scaling rules for the elemental stiffness relations, so that the irregular lattice is elastically homogeneous under uniform modes of straining. The elastically uniform lattice serves as a basis for the explicit modeling of heterogeneous features, such as short fibers.

(2) Fracture is modeled using a crack-band approach, where the crack band can form at arbitrary angles to the axes of the lattice elements. The dimensions of the crack band and the softening relation are also defined by the local geometry of the Voronoi diagram. Fracture localizes into the narrowest band permitted by lattice discretization and, therefore, the model can also be regarded as a cohesive zone representation of fracture.

(3) The crack-band representation of fracture involves an incremental softening of the lattice elements, according to the prescribed traction-displacement relation. This is in contrast to the conventional approach in which elements are completely removed from the lattice upon violating the fracture criterion.

(4) The fracture model is objective with respect to the irregular geometry of the lattice. During simulated fracture testing of a uniaxial tension specimen and a notched concrete beam, uniform fracture energy is consumed along the crack trajectory regardless of the mesh geometry. The common approach of assigning equal areas to the lattice elements, and the use of element axial forces to define the fracture criteria, leads to strongly nonuniform specific energy consumption along the crack path that, on the average, is much higher than that prescribed through the cohesive traction-displacement relation. Although disordered materials exhibit fluctuations in specific energy consumption as the fracture process advances, the fluctuations exhibited by the common lattice approach can be extreme and can bear no connection to the physical processes. This form of stress locking leads to overstrength and excess energy consumption in the global load-displacement response.

The fracture simulations presented in this paper involved statistically homogeneous softening materials as well as fiber-reinforced brittle-matrix composites. In the former case, the various sources of energy consumption during fracture were represented by a cohesive law. A similar approach can be applied in the fracture analysis of multiphase materials where each phase is assumed to be homogeneous. In the latter case, the stiffness, strength, and toughening mechanisms of individual fibers were explicitly represented within the material model. This enables the quantification and study of the effects of nonuniform fiber distributions on composite performance measures, such as postcracking strength and toughness. The explicit modeling of material structure, and its relations to system breakdown and failure, is a long-term objective of this research.

*Electronic address: jebolander@ucdavis.edu

†Electronic address: nsukumar@ucdavis.edu

[1] A. Hrennikoff, J. Appl. Mech. Tech. Phys. **12**, 169 (1941).

[2] H. J. Herrmann and S. Roux, eds., *Statistical Models for the Fracture of Disordered Media*, (North-Holland, Amsterdam, 1990).

[3] M. Sahimi, Phys. Rep. **306**, 213 (1998).

[4] M. Sahimi and J. D. Goddard, Phys. Rev. B **33**, 7848 (1986).

[5] P. D. Beale and D. J. Srolovitz, Phys. Rev. B **37**, 5500 (1988).

[6] S. Arbabi and M. Sahimi, Phys. Rev. B **47**, 695 (1993).

[7] G. N. Hassold and D. J. Srolovitz, Phys. Rev. B **39**, 9273 (1989).

[8] M. Sahimi and S. Arbabi, Phys. Rev. B **47**, 703 (1993).

[9] F. Tzschichholz, H. J. Herrmann, H. E. Roman, and M. Pfuff, Phys. Rev. B **49**, 7056 (1994).

[10] E. Schlangen and E. J. Garboczi, Int. J. Eng. Sci. **34**, 1131 (1996).

[11] A. Jagota and S. J. Bennison, in *Nonlinearity and Breakdown in Soft Condensed Matter*, Springer Lecture Notes in Physics Vol. 437, edited by K. K. Bardhan, B. K. Chakrabarti, and A. Hansen (Springer, Berlin, 1994), pp. 186–201.

[12] A. Jagota and S. J. Bennison, Modell. Simul. Mater. Sci. Eng. **3**, 485 (1995).

[13] N. H. Christ, R. Friedberg, and T. D. Lee, Nucl. Phys. B **210**, 337 (1982).

[14] A. Okabe, B. Boots, and K. Sugihara, *Spatial Tessellations: Concepts and Applications of Voronoi Diagrams* (John Wiley & Sons, Chichester, England, 1992).

[15] J. E. Bolander and S. Saito, Eng. Fract. Mech. **61**, 569 (1998).

[16] T. Kawai, Nucl. Eng. Des. **48**, 207 (1978).

[17] J. E. Bolander, K. Moriizumi, M. Kunieda, and M. Yip, in *Fracture mechanics of concrete structures* (AA Balkema Publishers, Lisse, The Netherlands, 2001), pp. 773–780.

[18] S. C. Harris, D. Williams, and R. Sibson, Math. Proc. Cambridge Philos. Soc. **125**, 535 (1999).

[19] N. Sukumar, Int. J. Numer. Methods Eng. **57**, 1 (2003).

[20] N. Sukumar and J. E. Bolander, Comput. Model. Eng. Sci. **4**, 691 (2003).

[21] E. Schlangen and J. G. M. van Mier, Cem. Concr. Compos. **14**, 105 (1992).

[22] Z. P. Bažant and B. H. Oh, Mater. Struct. **16**, 155 (1983).

[23] D. S. Dugdale, J. Mech. Phys. Solids **8**, 100 (1960).

[24] G. I. Barenblatt, Adv. Appl. Mech. **7**, 55 (1962).

[25] A. Hillerborg, M. Modeer, and P. E. Petersson, Cem. Concr. Res. **6**, 773 (1976).

[26] B. Lawn, *Fracture of Brittle Solids*, 2nd ed. (Cambridge University Press, Cambridge, England, 1993),

[27] H. L. Cox, Br. J. Appl. Phys. **3**, 72 (1952).

[28] Y. Kitsutaka, Y. Uchida, H. Mihashi, Y. Kaneko, S. Nakamura, and N. Kurihara, in *Fracture Mechanics of Concrete Structures* (AA Balkema Publishers, Lisse, The Netherlands, 2001), pp. 371–376.

[29] E. Schlangen and E. J. Garboczi, Eng. Fract. Mech. **57**, 319 (1997).

[30] P. Balaguru and S. P. Shah, *Fiber Reinforced Cement Composites* (McGraw-Hill, New York, 1992).

[31] A. E. Naaman, G. Namur, J. M. Alwan, and H. Najm, J. Eng. Mech. **117**, 2769 (1991).